J Therm Spray Tech (2026) 35:73–83
https://doi.org/10.1007/s11666-025-02114-0

ORIGINAL RESEARCH ARTICLE

A Modified Focused Ion-Beam Milling Approach to Reveal Subsurface Features of Plasma-Sprayed Ceramic Splats

Edward J. Gildersleeve V[1] · Emine Bakan[1] · Marcin Rasinksi[2] · Robert Vaßen[1]

Submitted: 22 April 2025 / in revised form: 28 August 2025 / Accepted: 15 October 2025 / Published online: 12 November 2025

Abstract This work presents a modified approach to Focused Ion Beam (FIB) milling, specifically tailored to preparing cross-sections of plasma sprayed resolidified ceramic splats, was developed at the Center for Thermal Spray Research at Stony Brook University and refined at the Forschungszentrum Jülich Thermal Spray Center. Two key advantages were gained from this modified approach: relatively large (100 µm long by 25-50 µm wide by 5-10 µm deep) ion-milled trenches were possible in as little as several hours of milling time and the traditional platinum overcoat was deemed not necessary. Images of single and double-splat cross-sections show the through-thickness crack propagation of mudflat cracks. Refinement of this method allowed for even shorter (up to or less than one hour) milling times for splat cross-section viewing, and concurrent Energy Dispersive Spectroscopy for chemical analysis of unique splat combinations of Thermal Barrier Coating (TBC) splats atop Environmental Barrier Coating (EBC) splats. Additionally, time-lapse imaging during the ion-milling process garnered additional insights about subsurface features within the splats. The results in this paper and the time-lapse animations online revealed subsurface 'bubbles' embedded in EBC splats—dependent on the process parameters. Finally, the TBC-on-EBC splat cross-section points toward the presence of viscous flow of solid amorphous EBC material during microsecond solidification of a molten TBC splat.

Keywords Focused Ion-Beam milling · Splats · YSZ · $Yb_2Si_2O_7$ · T-EBCs

This invited article is part of a special topical issue of the Journal of Thermal Spray Technology on 30 Years of Environmental Barrier Coatings. The issue was organized by Edward Gildersleeve, GE Aerospace, and Bryan Harder, NASA Glenn Research Center. Any views and opinions expressed in this article do not necessarily reflect those of the guest editors or their employers.

✉ Edward J. Gildersleeve V
Edward.gildersleeve.1@gmail.com

[1] Institute of Energy Materials and Devices, Materials Synthesis and Processing (IMD-2), Forschungszentrum Jülich GmbH., 52425 Jülich, Germany

[2] Institute of Fusion Energy and Nuclear Waste Management (IFN-1), Forschungszentrum Jülich GmbH., 52425 Jülich, Germany

Introduction

High-temperature ceramic barrier coatings by plasma spraying are a widely adopted technology in the power generation and propulsion industries (Ref 1-3). Presently, it is well-understood, most notably for Thermal Barrier Coatings (TBCs), that the microstructure and property of a plasma sprayed ceramic coating ties back to the mechanisms of droplet impact and solidification (Ref 4-12).

The impact of molten TBC material, in this case Yttria Stabilized Zirconia (YSZ), and its rapid solidification ($\sim 10^6$ K/s) generates quenching stresses that initiate and propagate through-thickness channel-cracks in the individual splats (Ref 4, 6, 8, 10, 13). Kulkarni et al. showed through high-resolution imaging that revealed nanoscale columnar grains in each individual splat, which were oriented in the solidification direction (Ref 14). It has also been shown that the shape and structure of these single splats has significant influence on the final property of the sprayed TBC (Ref 15-21). In some ways, TBC processing condition development has been driven by this understanding of the influence of the splat microstructure on the final quality of the coating (Ref 15-18). An example of this

is the literature's general agreement that fabricating Dense Vertically Cracked (DVC) TBCs requires a high deposition temperature combined with a high degree of particle melting—to enable optimal splat formation and stacking that yields a coating of sufficiently high stiffness during deposition, generating enough stored energy to induce the onset of vertical segmentation cracking (Ref 21-24). In understanding the process at a droplet/splat level, it has since been possible to expand TBC research outward—examining more advanced concepts e.g., the nonlinear elastic behavior of these coatings, phase distribution and stability at elevated temperatures, multi-layering, optimizing, and fabricating multifunctional TBCs, and so on (Ref 2, 22, 25-32).

Comparatively, Environmental Barrier Coatings (EBCs) for high-temperature ceramic components are not as thoroughly understood at the process-splat-microstructure level. EBCs are known to have higher sensitivity to input parameters (Ref 33, 34). This is especially true for rare earth disilicates (REDS), which undergo inflight chemical decomposition and rapidly solidify as amorphous, uncracked chemically heterogenous splats (Ref 33, 34). Thus, there is a need for advanced characterization techniques in this coatings space.

High-resolution microscopy studies using Focused Ion-Beam (FIB) milling methods to cross-section splats have been demonstrated in the thermal spray literature to elicit useful information about the deposition history of individual particles (Ref 35-43). However, these methods, upon their time of publication, had challenges. At the time of these publications, the FIB-milling methods were excessively long and induced some degree of redeposition/material sputtering during milling which made interpretation challenging (Ref 35-37). Contributing to the increased processing time was the sputtering of a platinum overlay coating prior to FIB-milling. Moreover, the majority of the available literature examines metallic splats or ceramics that are inapplicable as high-temperature barrier coatings.

In this work, a modified approach to traditional FIB milling was developed—specifically catered to high-throughput characterization of plasma-sprayed ceramic splats for TBCs and EBCs. First, the method was developed at the Center for Thermal Spray Research at Stony Brook University; then, refinement of the method was carried out at the Forschungszentrum Jülich Thermal Spray Center. Two important outcomes came from this reexamination of modern FIB-milling techniques. First, substantially larger cut areas (compared to any of the aforementioned literature) were deemed feasible at a fraction of the times reported in past literature. Second, through ion-beam optimizations, a platinum overlay coating was not required—thereby enhancing the quality of data that could be generated and interpretability of the resultant microstructures. Because of these method optimizations, key insights in the deposition dynamics of plasma-sprayed EBCs and Thermal-Environmental Barrier Coatings (T-EBCs) were ascertained.

Methods

Deposition of splats and their characterization were carried out across two facilities. For some work, the materials were plasma-sprayed at the Center for Thermal Spray Research (CTSR) at Stony Brook University, NY and subsequently characterized by FIB-SEM at Stony Brook University, NY. The remainder of the specimens were fabricated at the Forschungszentrum Jülich GmbH., IMD-2, at the Jülich Thermal Spray Center (JTSC) and characterized by FIB-SEM at the IFN-1 in Forschungszentrum Jülich. In all cases, the same working principles of ensuring optimal particle injection in the plasma spray torch, utilizing a high (>1500 mm/s) traverse rate of the torch across the sample, and low material feed rates to deposit splats were adopted. A combination of cascaded plasma and standard DC plasma torches were used to fabricate the splats shown in this study. The processing conditions used to fabricate the splats in this study were all reproduced from past literature by the authors (Ref 24, 33, 34, 44-48).

For these experiments, individual splats were deposited onto either mirror-polished 316L stainless steel (for the plasma-spray TBC baseline tests), mirror-polished silicon wafers (for the APS EBC tests), or mirror-polished plasma-sprayed coatings of $Yb_2Si_2O_7$ and Si (also for EBC testing). For the APS TBC spraying parameters, an F4MB standard DC plasma-spraying torch was used. For the APS EBC spraying parameters, a cascaded plasma torch [at Stony Brook SinplexPro™, Oerlikon Metco, Westbury NY; at Forschungszentrum Jülich, TriplexPro™, Oerlikon Metco, Wohlen Switzerland] was utilized with both argon-hydrogen (Ar-H_2) and argon-helium (Ar-He) plasma gases to study the effects of the plasma gas chemistries on the deposition of the individual splats. A summary of the APS deposition parameters are shown in Table 1.

After deposition, the specimens were gold-sputtered to achieve a coating of approximately 10-15 nm thickness (to avoid charging artifacts during the FIB-SEM analysis). The FIB-SEM used at Stony Brook was a LYRA-3 from Tescan [Tescan Group, a.s., Czech Republic]. Trial experiments on equivalent samples were carried out to study and understand the influence of the FIB-milling on splat integrity and morphology. For these experiments, the traditional platinum overcoat was intentionally avoided in order to allow investigations of the splat topography and the findings during FIB sectioning. The method and characterization

Table 1 Summary of APS deposition parameters (Ref 24, 33, 34, 44-48)

Condition	Argon flow rate, slpm	Hydrogen/helium^{+} flow rate, slpm	Spray current, Amp	Standoff distance, mm	Raster speed, mm/s
1[x,y] (TBCs)	47.5	6	550	60	1500
2[*,x] (EBC-A)	75	9	380	200	1500
3[*,x] (EBC-B)	75	9^{+}	480	200	1500
4[*,y] (EBC-C)	49	1	325	90	1500

[*]Cascaded plasma torch.

[x]Sprayed at Stony Brook University, CTSR.

[y]Sprayed at Forschungszentrum Jülich GmbH., JTSC.

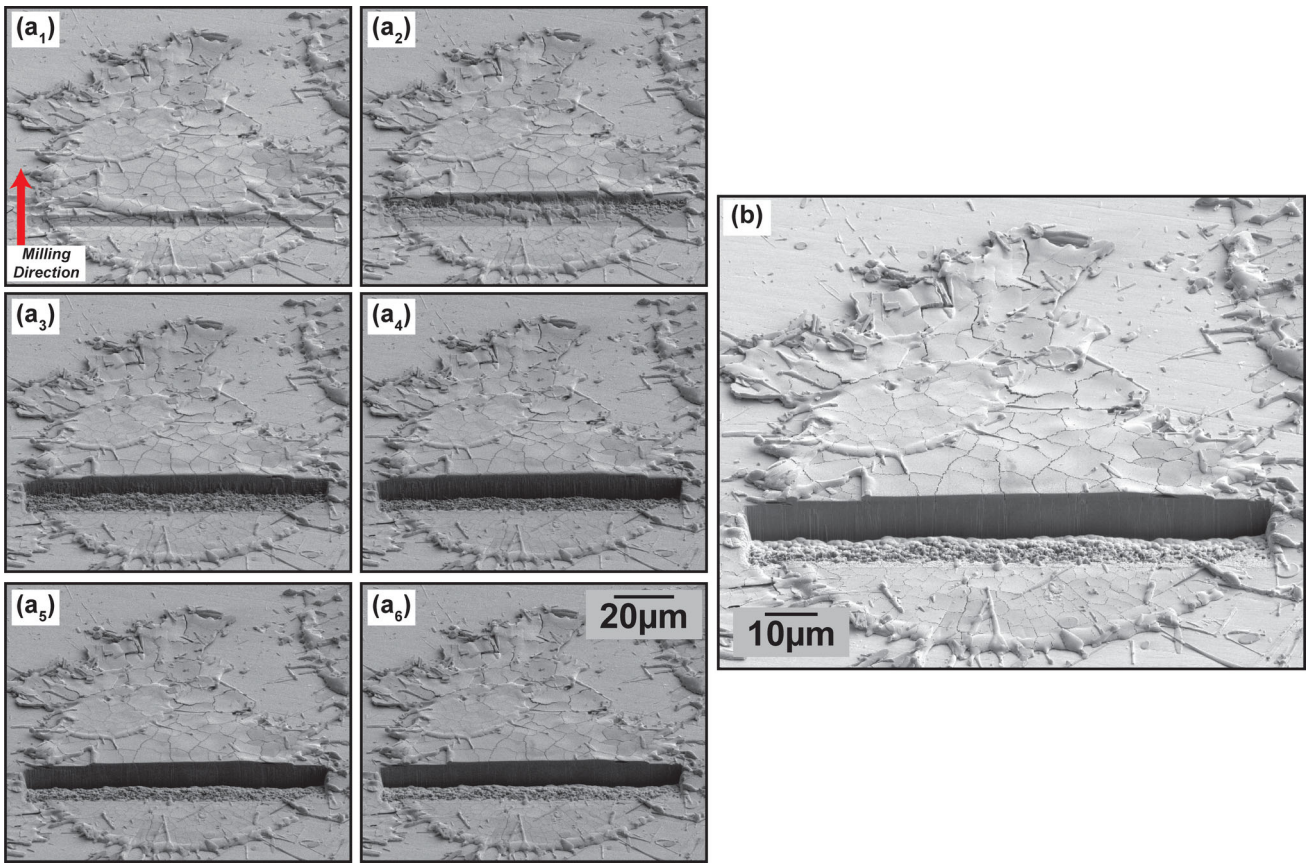

Fig. 1 Time-lapse images of the FIB-milling process for a 7YSZ splat deposited atop 316L stainless steel. (a_1–a_6) show iterative points along the ion-milling process, illustrating the trench cut (a_1–a_3), medium polish (a_4), and fine polish (a_5–a_6). A final macro-view SEM image of the milled splat is shown in (b). A time-lapse animation of this Figure is available online

techniques were further refined at the Forschungszentrum Jülich GmbH., IFN-1, using a Zeiss Crossbeam FIB-SEM.

As mentioned, unlike the previously published time-intensive FIB milling routines of past literature, the first iteration of the refined FIB-milling method at Stony Brook involved a multi-step (with each step being significantly quicker than predecessor methods due to increased ion currents) incremental milling routine. First, an ion current of 20nA was used to cut the 100 μm long × 15 μm wide × 5 μm deep trench. Then, sequentially, the trench-wall face was polished from 1nA, 500pA, 250pA, 100pA, 50pA, and finally 30pA for a final polishing step. Overall, the cross-sectioning routine for a ∼ 100 μm long × 15 μm wide × 5 μm deep trench took approximately 5 hours to complete. The milling was paused by an automated algorithm to take secondary electron images of the specimen in the process of cutting to gain further information. Figure 1 shows a time-lapse view of the ion-milling process (animation available online) at Stony Brook University. At intervals through the Fig. 1(e.g., a_2, a_3) one can see the quality of the

trench-wall is poorly defined due to resputtering and ion damage. The subsequent steps that this modified method proposes e.g., Fig. 1(a_4–a_6) are among the standout achievements of this method. At the Forschungszentrum Jülich, this FIB-milling method was further refined. The final FIB-milling parameters were divided into two processes, each using a different Ga ion beam current. The initial trench was cut with 30 kV 7nA beam, and was then further cleaned with 30 kV, 1.5nA beam. In total, the trench cuts and polishing amounted to a total of 45 to 60 minutes per cut. Unless otherwise stated in this paper, a platinum overlay coating was again foregone based off the learnings at the Stony Brook FIB-SEM.

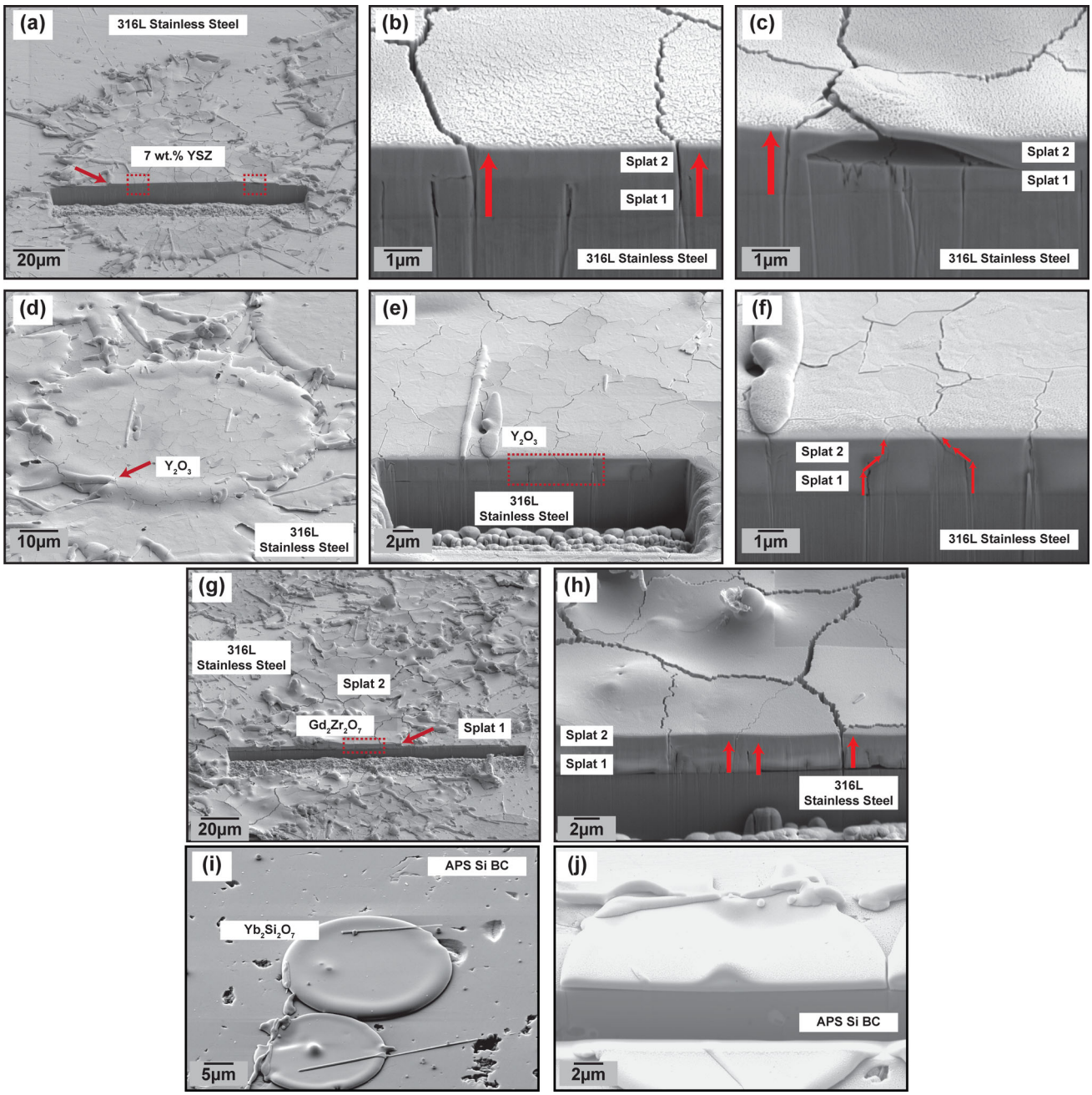

Fig. 2 Plasma-sprayed splats on representative substrates. (a–c) show 7 wt.% YSZ (d–f) show Y_2O_3 (g, h) show $Gd_2Zr_2O_7$. A set of $Yb_2Si_2O_7$ splats sprayed onto a silicon bond coat are shown in (i, j) for comparative purposes. Boxes indicate regions where high-magnification images were taken. Arrows in (a, d, g) indicate regions that show evidence that there are two successively deposited splats atop one another. Arrows in (b, c, f, h) trace the crack path in the cross-section

Results and Discussion

Baseline Microstructures: TBCs and $Yb_2Si_2O_7$ EBCs

Figure 2 shows the microstructure of several examples of APS ceramic splats deposited on representative substrates using processing conditions from Table 1. Many FIB cross-sections were conducted on all systems, and what is shown here are representative images of the overall findings. Unlike past FIB-splat studies, it is clear from the Figure that a platinum overlay coating was not needed to protect the surface from damage (Ref 12, 35-37). In addition, the ion-beam induced artifacts (extension of milling depth at crack sites, redeposition, edge-rollover) can clearly be seen as limited and constrained within only the substrate material. In other words, there was no evidence of milling-induced artifacts to change the appearance of the ceramic cross-sections. Figure 2 effectively serves as a reference for the remainder of the results shown in this study for what a 'baseline' FIB-milled splat microstructure would be for a given material system.

The Figure shows distinct differences in splat topography and cross-sectional microstructure which might be considered to be material-dependent. For instance, the crack-opening displacement (COD) of the through-thickness channel cracks in the 7 wt.% Yttria Stabilized Zirconia (7YSZ) and the Gadolinium Zirconate ($Gd_2Zr_2O_7$, GZO) are both considerably wider than the pure yttria (Y_2O_3) splats. This can especially be seen in all the high-magnification images. Moreover, Fig. 2(i), (j) shows plasma-sprayed $Yb_2Si_2O_7$ splats on a silicon bond coat—demonstrating as mentioned in the introduction that plasma-sprayed EBC splats do not have a tendency to crack.

In the three TBC/ceramic cases, the location of the cross-section is clearly one which contains multiple splats (likely two, assuming a splat thickness of 0.7-1.0 µm) successively deposited atop one another. From this, several observations can be made about the nature of mudflat cracking in successively deposited splats. In the case of 7YSZ and GZO, crack correlation seems to occur without significant bifurcation (Fig. 2b, h). Interestingly, in the case of Y_2O_3, the correlated cracking appears bifurcated at the interface between the two splats. Figure 2c shows an example wherein entrapped porosity between splats could inhibit correlated cracking.

These findings on the crack morphology of splats from different ceramics deposited on the same substrate material upon similar deposition conditions (similar deposition temperatures, particle states, etc.) also has important implications when considering the formation and growth of splat microcracks. If it is assumed the microcracks nucleate and open during rapid quenching, solidification, and ultimately cooldown to deposition temperature, where stresses are proportional to the thermal mismatch strains, $\sigma_{quench} \approx E\Delta\alpha\Delta T$, then 7YSZ, Y_2O_3, and GZO—with similar stiffnesses and thermal expansion coefficients—should exhibit similar microcrack features (Ref 6, 24, 44, 49). However, this is clearly not the case as shown in the Figure (i.e., different crack spacing, crack opening displacement, etc.).

Of course, this rudimentary analytical approach is limited, as it does not consider the energy release rates that drive microcracking nor the difference in fracture toughness, $\mathcal{G}_c$, values of the ceramic splats (Ref 25-27), which can influence the propensity and evolution of microcracks. Furthermore, this approach cannot accurately describe the stresses induced when a second splat is deposited onto a pre-solidified first splat. For this, it would be necessary to consider the heat transfer during second splat solidification and the complex stress states that arise from a fully-molten second splat landing atop a pre-cracked solid first splat. The analytical and finite element methods needed to ascertain this information are beyond the scope of this paper.

Observation of Embedded Porosity within Yb-Silicate Splats

Beyond the results shown by the FIB-milling process in Figure 2, a complimentary experiment was conducted at the Forschungszentrum Jülich wherein a similar plasma process was used to deposit fully-amorphous YbDS splats both on mirror-finished silicon bond coats and mirror-finished YbDS EBCs, shown in Fig. 3. It is important to identify that these two specimen shown here were sprayed at the exact same time in the same robot toolpath—and the position of the images taken relative to the sample surface are self-consistent i.e., geometrically centered within the spray plume. Thus, it is surmisable that the particles at this location shown in the images are (before impact) at nearly the same state.

From Fig. 3(a) and (a_1), some key insights can be drawn. First, the tendency for the YbDS splats to spread and channel-crack is higher when deposited atop YbDS as compared to Si. This could be due to the presence of underlying microcracks in the EBC where the splats impact—which could act as stress concentration sites to initiate channel-cracking of the splats during solidification (similar to what was observed in Fig. 2 with duplex crystalline ceramic splats). Second, the splats in Fig. 3(a) and (a_1), seem to show microscopic pores within the solidified droplets. Evidence of these 'nanopores' was identified by

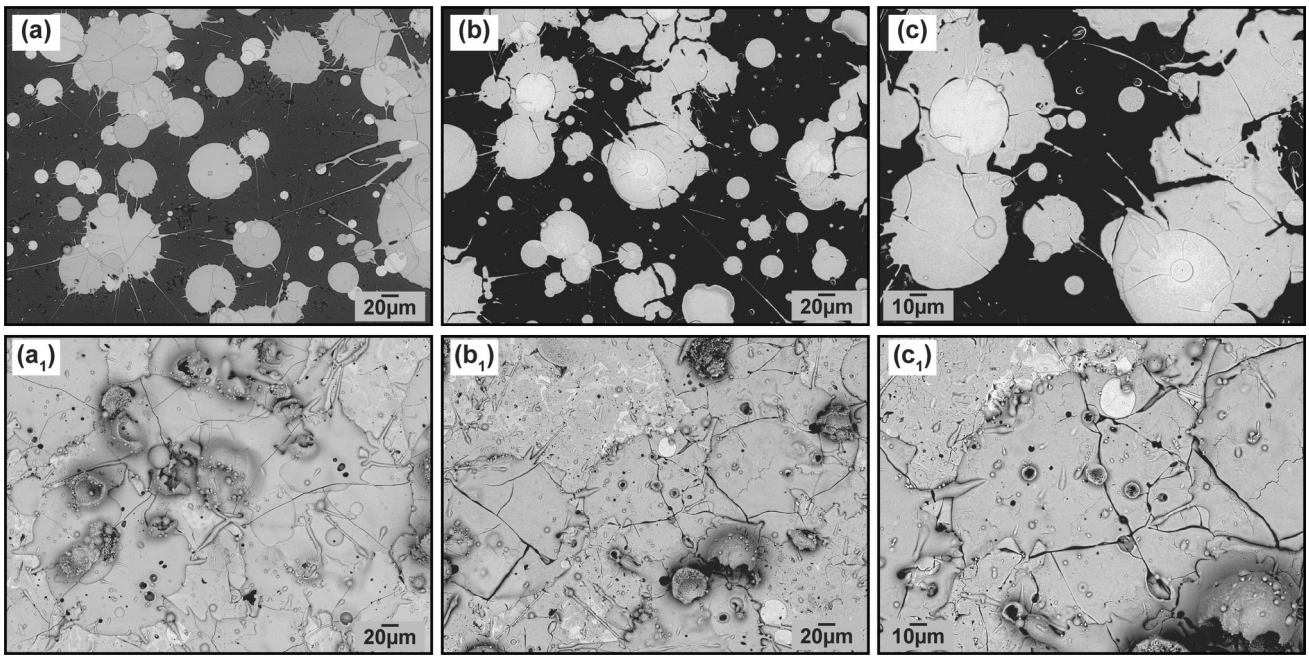

Fig. 3 $Yb_2Si_2O_7$ EBC splats sprayed on mirror-finished plasma-sprayed Si bond coats (a, b, c) and mirror-finished $Yb_2Si_2O_7$ EBC coatings (a_1, b_1, c_1). Both the as-sprayed (a, a_1) and crystallized/heat-treated (b, b_1, c, c_1) splats are shown here. The same sample was utilized for all images

Qu et al. when examining metallic Ni splats on preheated stainless steel substrates (Ref 50, 51). In these studies, the authors theorize the molten droplets are entrapping gas inflight, and then upon impact, depressurization leads to rapid nucleation of bubbles at the splat/substrate interface (Ref 50, 51). Since then, numerical and high-resolution imaging investigations of the phenomenon have validated some of these hypotheses (Ref 52, 53).

Comparing Fig. 3(a) with Fig. 3(a_1), the pore area fraction and pore shape on the EBC splats appears to change. This could be related with the higher thermal conductivity of Si relative to the EBC, enhancing the heat transfer from the molten YbDS splat thereby increasing the cooling and solidification rate before most of entrapped gases can escape. Similarly, Qu et al. showed when spraying Ni on Cu substrates, the nanopores decreased in size, presumably due to the higher thermal conductivity of the substrate enhancing the solidification rate and thereby inhibiting bubble coagulation (Ref 50).

When the amorphous splats are crystallized (Fig. 3b, b_1, c, c_1), they exhibit stresses (likely due to constrained volume change) which drive delamination/peeling when on silicon bond coats, but conversely drive increased COD when sprayed onto YbDS directly. Figure 2(j) clearly demonstrates that despite the seemingly-good adherence of YbDS splats on mirror-finished Si bond coats, they are already pre-delaminated at the splat edges. Moreover, the individual crystallized YbDS splats each have a unique grain structure and backscatter contrast, especially in Fig. 3(c), which is assumed to be a consequence of the inflight chemical shift.

From the results of Fig. 2(i), (j) and 3, an easy misinterpretation would be that the first YbDS splats sprayed on Si are intrinsically denser than their subsequent counterparts. However, this could be misleading especially in viewing the FIB-milled splat in Fig. 2(j), due to the possibility of redeposition/re-sputtering of material during ion milling. Time-lapse imaging during milling of plasma-sprayed EBC splats sprayed at Stony Brook revealed otherwise hidden features.

Figure 4 and 5 show time-lapse progressions of the FIB-milling process done on single APS ytterbium disilicate ($Yb_2Si_2O_7$, YbDS) splats. Animations of these time-lapse millings are available online. It is assumed these two splats shown should be equivalently amorphous due to equivalent solidification rates (Ref 33, 34). These two splats also are deposited from plasma plumes of equivalent molten content (Ref 54). From the two Figures, it would seem the processing gas mixtures play an important role on the intrinsic microstructure of the individual splats. In the case of the Ar-H_2 splat, there is significantly less embedded/entrapped porosity than in the case of the Ar-He splat. Furthermore, from the top-surface viewing before milling, the splats observed in Fig. 4(a) and 5(a) are morphologically quite similar (no cracking and no presence of unmolten/semimolten particulates within the splats).

Thus, if the particle temperatures/velocities were the same, and if the deposition temperatures were the same, the

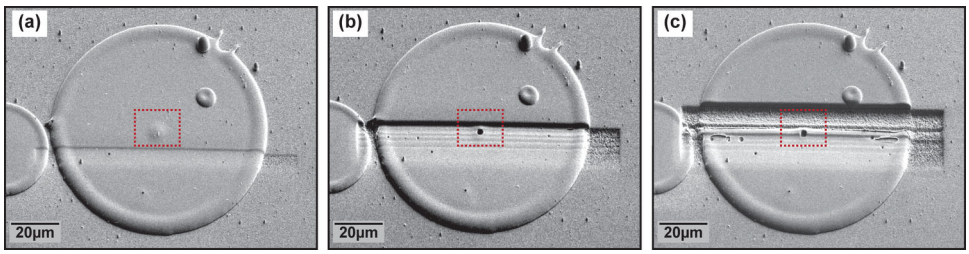

Fig. 4 Time-lapsed SEM images of APS Ar-H_2 ytterbium disilicate ($Yb_2Si_2O_7$) splats deposited on mirror-polished Si wafers. (a–c) show the progression in time during FIB milling, revealing entrapped porosity. The direction of ion-beam milling in the images is moving toward the top of the image

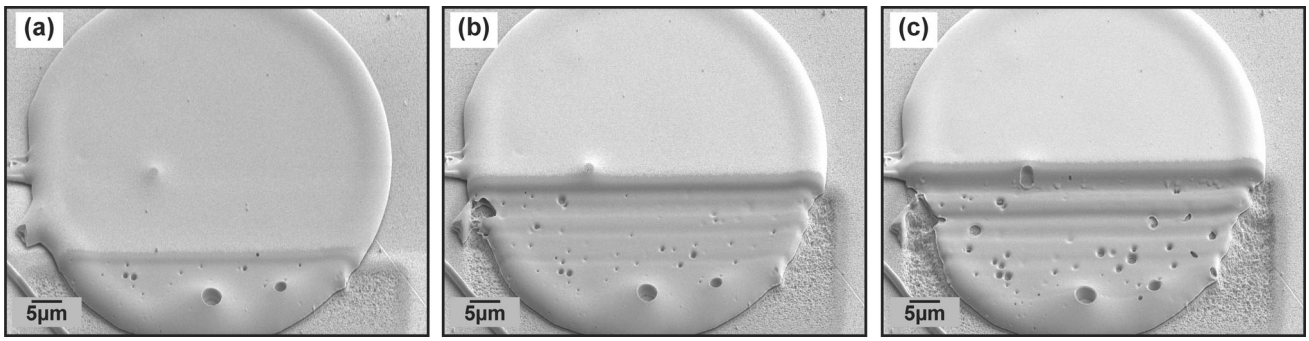

Fig. 5 Time-lapsed SEM images of APS Ar-He ytterbium disilicate ($Yb_2Si_2O_7$) splats deposited on mirror-polished Si wafers. (a–c) show the progression in time during FIB milling, revealing entrapped porosity. The direction of ion-beam milling in the images is moving toward the top of the image

only substantial difference in the deposition conditions to be noted here is the presence (or lack) of hydrogen in the plasma gas mixture. Therefore, it seems clear that when using Ar-He plasmas, there is a higher tendency to observe splats with significantly higher embedded porosity.

The approach outlined by Qu et al. and followed by Han et al. imply a sensitivity of bubble retention and formation to melt viscosity (Ref 50-52). In the case of a plasma-sprayed Ni splat, it is reasonable to assume a single value for viscosity. However, in the case of plasma-sprayed silicates, there is a higher propensity for individual droplet-to-droplet chemical shift (also visible in Fig. 3). Those droplets which are SiO_2-lean would be supposed to have less viscosity compared to their SiO_2-rich counterparts. Consequentially, as described by Qu et al., these lower-viscosity (more volatilized, SiO_2-lean) melts would be more prone to outwardly diffuse gas (Ref 50, 51). This might explain why the Ar-H_2 splats are significantly less porous than the Ar-He counterparts, however there are also differences in the viscosity of gaseous H_2 and He in molten magmatic silicates that should be considered in future research on this topic (Ref 55-58). Nevertheless, this is a fundamental research problem that has direct implications on the microstructure of EBCs and warrants further dedicated study.

Observation of Viscous Flow During Impact and Solidification of Molten 7YSZ on Amorphous $Yb_2Si_2O_7$

Recently, it has been shown that despite high-CTE mismatch strains, it is possible to plasma-spray a TBC atop an EBC if and only if the underlying EBC is amorphous prior to spraying the TBC (Ref 45, 59). The working hypothesis as to what drives this enhanced cohesion between TBC and EBC is a rapid interdiffusion of ionic species during TBC rapid solidification. However, there is limited proof to support this at present. An experiment using this modified ion-milling approach was carried out in an attempt to support the interdiffusion hypothesis.

Figure 6 shows the microstructure of a plasma-sprayed TBC splat deposited atop a preexisting amorphous YbDS EBC splat, all atop a silicon bond coat. Evidently from the Figure, there are massive CTE-driven strains during cool-down to room temperature that cause the 7YSZ splat to 'lift' off the substrate material. However, even in Fig. 6(a_1), (a_2), from a top-down view, a distinct bright-phase can be seen protruding along a surface crack. Tilted secondary electron imaging in Fig. 6(b_1), (b_2) also support the evidence of a secondary species protruding through the surface crack. Upon FIB-sectioning the material (Fig. 6c1, c2), it becomes clear that indeed the underlying YbDS

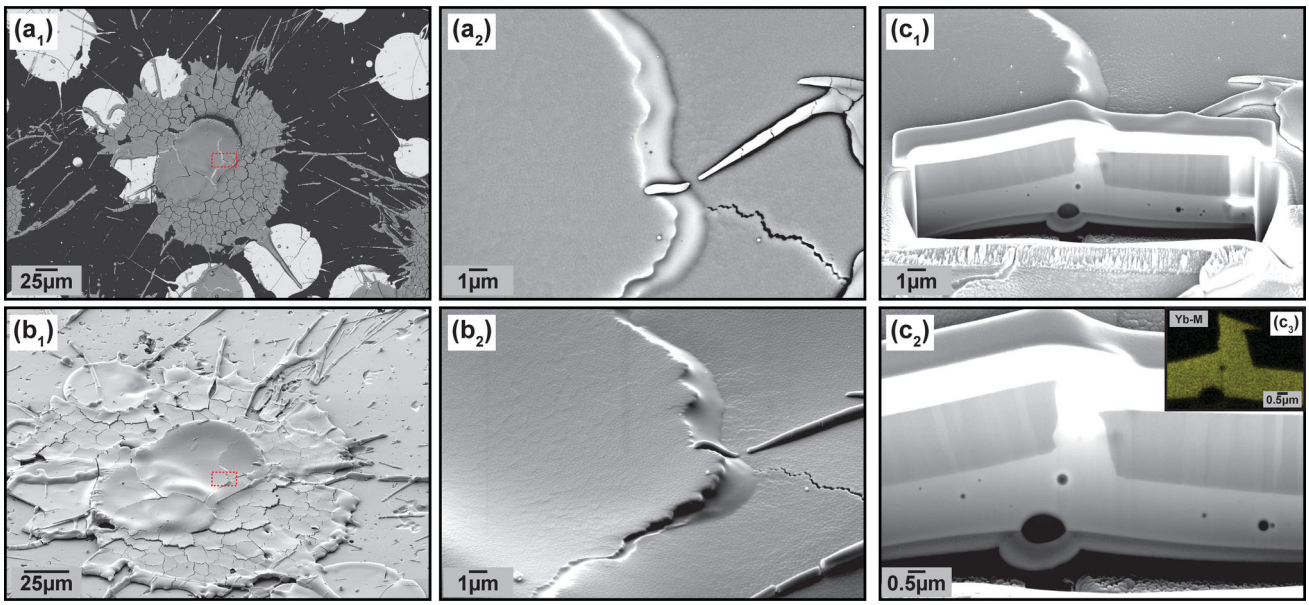

Fig. 6 7YSZ splat plasma-sprayed atop amorphous $Yb_2Si_2O_7$ splats atop a mirror-polished silicon bond coat (a, b_1). A high-magnification view of the glass-protrusion is shown in backscatter in a_2 and secondary imaging in b_2. (c_1, c_2) show the final FIB cross-section of this location of interest is shown in InLens mode. A platinum overlay coating was applied to this cross-section to protect the integrity of the protruding glass through the 7YSZ splat crack. A Yb-M EDS Map taken at 8 kV accelerating voltage at the same magnification as (c_2) is shown for reference in (c_3)

amorphous splat was essentially 'pulled' or extruded into the crack developed in the 7YSZ splat.

Some literature suggests that for silicate melts/glasses, the relative rate of temperature change as a function of time can substantially influence the change in viscosity. Subsequently as the silicate becomes less viscous and more mobile, it becomes subjected to 'viscous heating' due to the sudden release of stored energy in the system (Ref 60-62). This is the crux of the working hypothesis of what drives the observed cross-section seen in Fig. 6. The impacting molten 7YSZ splat transfers its heat during solidification to the underlying glassy YbDS splat, rapidly raising it toward its glass transition temperature T_g and 'extruding' the less-viscous-solid wherever there is open space. The extrusion subsequently further raises the glass temperature by viscous heating, but evidently not to an extent wherein the glassy material crystallizes and becomes immobile. A Yb-M EDS map taken at the same location is shown in Fig. 6(c_3) to illustrate the viscous mobility of the YbDS splat upon 7YSZ impact.

EDS analysis also showed that there is the presence of Zr (not shown here) within the protruding glass, in between the two zones of 7YSZ splat material—suggesting and corroborating the interdiffusion theory. The FIB-sectioning also revealed that the cohesive integrity is quite high between the 7YSZ and amorphous YbDS, despite the clearly large strains causing the material to physically lift off the substrate. Finally, embedded and entrapped porosity in the amorphous YbDS splat can again be seen, in corroboration with what has been shown throughout this study. As in the prior case studies, the refinement of a modified FIB milling approach, specifically catered toward the preservation of individual thermally-sprayed splats, has allowed otherwise unattainable insight toward one of the key driving mechanisms of adhesion between a TBC material plasma-sprayed onto an amorphous EBC.

Conclusions

This work has demonstrated the development of a new approach to conventional Focused Ion-Beam milling. Using this modified approach, it is possible to elucidate meaningful information from plasma-sprayed splats that would otherwise not be known. Unlike traditional FIB-milling, it was shown here that a platinum overlay is not usually required—which is advantageous to the experimentalist in allowing the correlation between surface and cross-sectional features (i.e., microcracking). Additionally, this modified approach has further advantages in that high-quality cross-sections of splats can be obtained in significantly less processing time than past studies that have explored this technique.

The findings in this work have shown that in polycrystalline TBC ceramics, there is a tendency for splat-to-splat microcrack correlation during successive impact and solidification. The correlation of through-thickness microcracking in successively deposited splats was also seen to

be material-dependent. In addition, this modified FIB-milling methodology unveiled unexpected insights on one source of porosity in APS EBCs. When examining Ar-H_2 and Ar-He sprayed ytterbium silicate splats, it was found that the Ar-He splats retain a significantly higher amount of embedded porosity. This was theorized to be in relation to the viscosity and diffusion coefficients of inert gases in silicate melts—that helium has a significantly higher diffusivity than other gases. Further splat analysis of plasma-sprayed EBC coated systems from different sites and by different methods supported the assumption of process gas entrapment.

It was also shown that this modified FIB-milling/SEM-EDS approach can offer advantageous analytical tools to characterize new and emerging coatings such as Thermal-Environmental Barrier Coatings. With this technique, the interdiffusion of species during deposition can be better characterized.

Ultimately this study strives to serve as a framework to inspire future works that may utilize this modified technique to gain meaningful information from their processes about the fundamental formation dynamics of thermally-sprayed coatings. Not shown here due to lack of available data was a side-by-side comparison of the "more conventional" milling methods with this new modified method. Future work could focus on previously analyzed systems e.g., those referenced in this article—revisited with this modified milling method. In revisiting, new conclusions about the formation dynamics of these systems due to the minimization of a Heat Affected Zone and/or redeposition by ion milling might be garnered. Conceivably, this modified technique could be transferred to any type of rapidly quenched droplet on a substrate and is not limited to plasma-sprayed ceramic splats.

Supplementary Information The online version contains supplementary material available at https://doi.org/10.1007/s11666-025-02114-0.

Acknowledgments Funding by the Industrial Consortium for Thermal Spray Technology is gratefully acknowledged. Partial funding by the Alexander von Humboldt Foundation for a portion of this work is gratefully acknowledged. Technical assistance and support by Lucille Giannuzi and S. Sharang at TESCAN during the experiments is also appreciated.

Funding Open Access funding enabled and organized by Projekt DEAL.

References

1. A. Vardelle, C. Moreau, J. Akedo, H. Ashrafizadeh, C.C. Berndt, J.O. Berghaus, M. Boulos, J. Brogan, A.C. Bourtsalas, A. Dolatabadi, M. Dorfman, T.J. Eden, P. Fauchais, G. Fisher, F. Gaertner, M. Gindrat, R. Henne, M. Hyland, E. Irissou, E.H. Jordan, K.A. Khor, A. Killinger, Y.-C. Lau, C.-J. Li, L. Li, J. Longtin, N. Markocsan, P.J. Masset, J. Matejicek, G. Mauer, A. McDonald, J. Mostaghimi, S. Sampath, G. Schiller, K. Shinoda, M.F. Smith, A.A. Syed, N.J. Themelis, F.-L. Toma, J.P. Trelles, R. Vassen and P. Vuoristo, The 2016 Thermal Spray Roadmap, *J. Therm. Spray Technol.*, 2016, **25**(8), p 1376–1440.
2. S. Sampath, U. Schulz, M.O. Jarligo and S. Kuroda, Processing Science of Advanced Thermal-Barrier Systems, *MRS Bull.*, 2012, **37**(10), p 903–910.
3. R. Vaßen, E. Bakan, D.E. Mack and O. Guillon, A Perspective on Thermally Sprayed Thermal Barrier Coatings: Current Status and Trends, *J. Therm. Spray Technol.*, 2022, **31**(4), p 685–698.
4. L. Bianchi, A.C. Leger, M. Vardelle, A. Vardelle and P. Fauchais, Splat Formation and Cooling of Plasma-Sprayed Zirconia, *TSF*, 1997, **305**(1), p 35–47.
5. G. Montavon, S. Sampath, C.C. Berndt, H. Herman and C. Coddet, Effects of the Spray Angle on Splat Morphology During Thermal Spraying, *Surf. Coat. Technol.*, 1997, **91**(1), p 107–115.
6. Y.C. Tsui and T.W. Clyne, An Analytical Model for Predicting Residual Stresses in Progressively Deposited Coatings Part 1: Planar Geometry, *TSF*, 1997, **306**(1), p 23–33.
7. A. Vardelle, C. Moreau and P. Fauchais, The Dynamics of Deposit Formation in Thermal-Spray Processes, *MRS Bull.*, 2000, **25**(7), p 32–37.
8. S. Sampath and X. Jiang, Splat Formation and Microstructure Development During Plasma Spraying: Deposition Temperature Effects, *Mater. Sci. Eng. A*, 2001, **304–306**, p 144–150.
9. H. Zhang, X.Y. Wang, L.L. Zheng and X.Y. Jiang, Studies of Splat Morphology and Rapid Solidification During Thermal Spraying, *Int. J. Heat Mass Transfer*, 2001, **44**(24), p 4579–4592.
10. M. Pasandideh-Fard, V. Pershin, S. Chandra and J. Mostaghimi, Splat Shapes in a Thermal Spray Coating Process: Simulations And Experiments, *J. Therm. Spray Technol.*, 2002, **11**(2), p 206–217.
11. H. Zhang, H.B. Xiong, L.L. Zheng, A. Vaidya, L. Li and S. Sampath, Melting Behavior of In-Flight Particles and Its Effects on Splat Morphology in Plasma Spraying, ASME, *Int. Mech. Eng. Congr. Expositioned.*, 2002, **2002**, p 309–316.
12. L. Li, B. Kharas, H. Zhang and S. Sampath, Suppression of Crystallization During High Velocity Impact Quenching of Alumina Droplets: Observations and Characterization, *Mater. Sci. Eng. A*, 2007, **456**(1), p 35–42.
13. H. Herman, S. Sampath and R. McCune, Thermal Spray: Current Status and Future Trends, *MRS Bull.*, 2000, **25**(07), p 17–25.
14. A. Kulkarni, A. Vaidya, A. Goland, S. Sampath and H. Herman, Processing Effects on Porosity-Property Correlations in Plasma Sprayed Yttria-Stabilized Zirconia Coatings, *Mater. Sci. Eng. A*, 2003, **359**(1), p 100–111.
15. Y. Liu, T. Nakamura, V. Srinivasan, A. Vaidya, A. Gouldstone and S. Sampath, Non-Linear Elastic Properties of Plasma-Sprayed Zirconia Coatings and Associated Relationships with Processing Conditions, *Acta Mater.*, 2007, **55**(14), p 4667–4678.

16. W. Chi, S. Sampath and H. Wang, Microstructure-Thermal Conductivity Relationships for Plasma-Sprayed Yttria-Stabilized Zirconia Coatings, *J. Am. Ceram. Soc.*, 2008, **91**(8), p 2636–2645.
17. Y. Liu, T. Nakamura, G. Dwivedi, A. Valarezo and S. Sampath, Anelastic Behavior of Plasma-Sprayed Zirconia Coatings, *J. Am. Ceram. Soc.*, 2008, **91**(12), p 4036–4043.
18. A.T.T. Tran, M.M. Hyland, K. Shinoda and S. Sampath, Influence of Substrate Surface Conditions on the Deposition and Spreading of Molten Droplets, *TSF*, 2011, **519**(8), p 2445–2456.
19. R. Vaßen, N. Czech, W. Malléner, W. Stamm and D. Stöver, Influence of Impurity Content and Porosity of Plasma-Sprayed Yttria-Stabilized Zirconia Layers on the Sintering Behaviour, *Surf. Coat. Technol.*, 2001, **141**(2), p 135–140.
20. R. Vaßen, G. Kerkhoff and D. Stöver, Development of a Micromechanical Life Prediction Model for Plasma Sprayed Thermal Barrier Coatings, *Mater. Sci. Eng. A*, 2001, **303**(1), p 100–109.
21. H.B. Guo, R. Vaßen and D. Stöver, Atmospheric Plasma Sprayed Thick Thermal Barrier Coatings with High Segmentation Crack Density, *Surf. Coat. Technol.*, 2004, **186**(3), p 353–363.
22. H. Guo, S. Kuroda and H. Murakami, Microstructures and Properties of Plasma-Sprayed Segmented Thermal Barrier Coatings, *J. Am. Ceram. Soc.*, 2006, **89**(4), p 1432–1439.
23. G.-J. Yang, C.-X. Li, S. Hao, Y.-Z. Xing, E.-J. Yang and C.-J. Li, Critical Bonding Temperature for the Splat Bonding Formation During Plasma Spraying of Ceramic Materials, *Surf. Coat. Technol.*, 2013, **235**, p 841–847.
24. S.V. Shinde, E.J. Gildersleeve, C.A. Johnson and S. Sampath, Segmentation Crack Formation Dynamics During Air Plasma Spraying of Zirconia, *Acta Mater.*, 2020, **183**, p 196–206.
25. C. Mercer, J.R. Williams, D.R. Clarke and A.G. Evans, On a Ferroelastic Mechanism Governing the toUghness of Metastable Tetragonal-Prime (t′) Yttria-Stabilized Zirconia, *Proc. R. Soc A Math. Phys. Eng. Sci.*, 2007, **463**(2081), p 1393–1408.
26. E.M. Donohue, N.R. Philips, M.R. Begley and C.G. Levi, Thermal Barrier Coating Toughness: Measurement and Identification of a Bridging Mechanism Enabled by Segmented Microstructure, *Mater. Sci. Eng. A*, 2013, **564**, p 324–330.
27. G. Dwivedi, V. Viswanathan, S. Sampath, A. Shyam and E. Lara-Curzio, Fracture Toughness of Plasma-Sprayed Thermal Barrier Ceramics: Influence of Processing, Microstructure, and Thermal Aging, *J. Am. Ceram. Soc.*, 2014, **97**(9), p 2736–2744.
28. E. Bakan, D.E. Mack, G. Mauer and R. Vaßen, Gadolinium Zirconate/YSZ Thermal Barrier Coatings: Plasma Spraying, Microstructure, and Thermal Cycling Behavior, *J. Am. Ceram. Soc.*, 2014, **97**(12), p 4045–4051.
29. R. Vaßen, E. Bakan, D. Mack, S. Schwartz-Lückge, D. Sebold, Y. Jung Sohn, D. Zhou and O. Guillon, Performance of YSZ and Gd2Zr2O7/YSZ Double Layer Thermal Barrier Coatings in Burner Rig Tests, *J. Eur. Ceram. Soc.*, 2020, **40**(2), p 480–490.
30. D. Zhou, D.E. Mack, E. Bakan, G. Mauer, D. Sebold, O. Guillon and R. Vaßen, Thermal Cycling Performances of Multilayered Yttria-Stabilized Zirconia/Gadolinium Zirconate Thermal Barrier Coatings, *J. Am. Ceram. Soc.*, 2020, **103**(3), p 2048–2061.
31. V. Viswanathan, G. Dwivedi and S. Sampath, Engineered Multilayer Thermal Barrier Coatings for Enhanced Durability and Functional Performance, *J. Am. Ceram. Soc.*, 2014, **97**(9), p 2770–2778.
32. V. Viswanathan, G. Dwivedi and S. Sampath, Multilayer, Multimaterial Thermal Barrier Coating Systems: Design, Synthesis, and Performance Assessment, *J. Am. Ceram. Soc.*, 2015, **98**(6), p 1769–1777.
33. E. Bakan, D. Marcano, D. Zhou, Y.J. Sohn, G. Mauer and R. Vaßen, Yb2Si2O7 Environmental Barrier Coatings Deposited by Various Thermal Spray Techniques: A Preliminary Comparative Study, *J. Therm. Spray Technol.*, 2017, **26**(6), p 1011–1024.
34. E. Garcia, H. Lee and S. Sampath, Phase and Microstructure Evolution in Plasma Sprayed Yb2Si2O7 Coatings, *J. Eur. Ceram. Soc.*, 2019, **39**(4), p 1477–1486.
35. P.C. King, S.H. Zahiri and M. Jahedi, Focused Ion Beam Micro-Dissection of Cold-Sprayed Particles, *Acta Mater.*, 2008, **56**(19), p 5617–5626.
36. G. Bolelli, K. Sabiruddin, L. Lusvarghi, E. Gualtieri, S. Valeri and P.P. Bandyopadhyay, FIB Assisted Study of Plasma Sprayed Splat–Substrate Interfaces: NiAl–Stainless Steel and Alumina–NiAl Combinations, *Surf. Coat. Technol.*, 2010, **205**(2), p 363–371.
37. Y. Wu, M. Qu, L. Gianuzzi, S. Sampath and A. Gouldstone, Focused Ion Beam Study of Ni5Al Single Splat Microstructure, *MRS Online Proc. Libr.*, 2007, **983**(1), p 404.
38. K. Kim, M. Watanabe, S. Kuroda and N. Kawano, Observation of High Resolution Microstructures in Advanced Thermal Sprayed Coatings and Single Deposited Splats Using Ion Beam Milling, *J. Vacuum Soc. Japan*, 2013, **56**(8), p 291–297.
39. Y. Zhang, S. Matthews and M. Hyland, Understanding the Formation of Plasma-Sprayed Ni20Cr Splats Through Interface Observation, *ApSS*, 2019, **469**, p 691–702.
40. A. McDonald, S. Chandra and C. Moreau, Photographing Impact of Plasma-Sprayed Particles on Rough Substrates, *JMatS*, 2008, **43**(13), p 4631–4643.
41. H.R. Salimijazi, L. Pershin, T.W. Coyle, J. Mostaghimi, L. Rosenzweig and E. Moran, Effect of Substrate Temperature and Droplet Characteristics on Plasma Sprayed Zirconia Splats, *ITSC2006ed*, 2006, **2006**, p 483–488.
42. D. McGrouther and P.R. Munroe, Imaging and Analysis of 3-D Structure Using a Dual Beam FIB, *Microsc. Res. Tech.*, 2007, **70**(3), p 186–194.
43. S. Brossard, P.R. Munroe, A. Tran and M.M. Hyland, Study of the Splat-Substrate Interface for a NiCr Coating Plasma Sprayed onto Polished Aluminum and Stainless Steel Substrates, *J. Therm. Spray Technol.*, 2010, **19**(1), p 24–30.
44. S.V. Shinde and S. Sampath, Factors Governing Segmentation Crack Characteristics in Air Plasma Sprayed Ceramics, *J. Eur. Ceram. Soc.*, 2022, **42**(3), p 1077–1087.
45. E.J. Gildersleeve, E. Bakan and R. Vaßen, Integrating State of the Art Zirconia Thermal Barriers with Ytterbium Silicate Environmental Barriers for Silicon-Based Ceramic Turbine Components, *J. Therm. Spray Technol.*, 2023, **33**, p 195.
46. E.J. Gildersleeve V, E. Bakan, R. Vassen, *MultiLayered Thermal-Environmental Barrier Coatings (T-EBCs) for Future Ceramic Turbine Components: An Assessment of Feasibility and Efficacy,* International Thermal Spray Conference 2024, Milan, IT, 2024
47. E. Bakan, E.J. Gildersleeve and R. Vaßen, Towards Highly Dense Yb-Silicate Microstructures Deposited by Air Plasma Spray for Environmental Barrier Coating Applications I: Influence of Local Deposition Rate, *J. Therm. Spray Technol.*, 2025, **34**, p 1452.
48. E.J. Gildersleeve, E. Bakan and R. Vaßen, Towards Highly Dense Yb-Silicate Microstructures Deposited by Air Plasma Spray for Environmental Barrier Coating Applications II: Plasma Gas Composition, Feedstock, and Anode Orifice Comparisons, *J. Therm. Spray Technol.*, 2025, **34**, p 1452.
49. S.V. Shinde and S. Sampath, Interplay Between Cracking and Delamination in Incrementally Deposited Plasma Sprayed Coatings, *Acta Mater.*, 2021, **215**, 117074.
50. M. Qu, Y. Wu, V. Srinivasan and A. Gouldstone, Observations of Nanoporous Foam Arising from Impact and Rapid Solidification of Molten Ni Droplets, *Appl. Phys. Lett.*, 2007, **90**(25), 254101.
51. M. Qu and A. Gouldstone, On the Role of Bubbles in Metallic Splat Nanopores and Adhesion, *J. Therm. Spray Technol.*, 2008, **17**(4), p 486–494.

52. H. Ge, K. Wang, J. Chen, R. Zhu, M. Lazarus and D. Yan, Numerical Investigation of Air Entrapment Dynamics for High-Speed Thermal Spraying, *Appl. Sciencesed.*, 2022, **12**, p 12039.
53. J.S. Lee, B.M. Weon, J.H. Je and K. Fezzaa, How Does an Air Film Evolve into a Bubble During Drop Impact?, *Phys. Rev. Lett.*, 2012, **109**(20), 204501.
54. E.J. Gildersleeve, E. Garcia and S. Sampath, Plasma Gas Chemistry Effects on the In-Flight Stoichiometric Changes of Ytterbium Silicate EBCs, *J. Therm. Spray Technol.*, 2025, **1**, p 18.
55. J.M. Bockris and D. Lowe, Viscosity and the Structure of Molten Silicates, *Proc. R. Soc. Lond. A*, 1954, **226**(1167), p 423–435.
56. Y. Bottinga and D.F. Weill, The Viscosity of Magmatic Silicate Liquids; a Model Calculation, *Am. J. Sci.*, 1972, **272**(5), p 438–475.
57. A.W.H. Mann, *Diffusion in Natural Silicate Melts: a Critical Review*, Princeton University Press Princeton, NJ, 1980.
58. H.R. Shaw, *Diffusion of H2O in Granitic Liquids: Part I. Experimental Data; Part II. Mass Transfer in Magma Chambers, Geochemical Transport and Kineticsed*, Carnegie Inst., Washington Publ, 1974, p 139–170
59. E.J. Gildersleeve, E. Bakan, M. Rasinski, M. Kindelmann, A. Vayyala, E. Wessel, J. Mayer and R. Vaßen, Unveiling Microsecond Diffusion Bonding Phenomena Enabled by Air Plasma Spraying Zirconia Thermal Barrier Ceramics onto Rare Earth Environmental Barrier Silicates, *Sci. Rep.*, 2025, **15**(1), p 27031.
60. K.-U. Hess, B. Cordonnier, Y. Lavallée and D.B. Dingwell, Viscous Heating in Rhyolite: An in situ Experimental Determination, *Earth Planet. Sci. Lett.*, 2008, **275**(1), p 121–126.
61. W. Zhu, Y. Xia, B.G. Aitken and S. Sen, Temperature Dependent Onset of Shear Thinning in Supercooled Glass-Forming Network Liquids, *J. Chem. Phys.*, 2021, **154**(9), 094507.
62. S. Okumura, K. Uesugi, A. Goto, K. Matsumoto and T. Sakamaki, A Molecular-Scale Origin of Shear Thinning and Brittle Failure of Silicate Melt, *GeoRL*, 2023, **50**(16), p e2023GL104083.